V J Smith

H H Wills Physics Laboratory

University of Bristol

BRISTOL PHYSICS

Experiments with Hyperon Beams at the CERN SPS

Hyperon99 Symposium: Fermilab, September 27 1999

Hyperon99 - Historical Overview

(1) Hyperons are baryons containing at least one (valence) <u>strange quark</u>.

(1a) Hyperons have spin.

(2) Hyperons decay by the weak interaction:

(2a) Hyperons have mean lives of order 10^{-10} s

(few cm $\rightarrow$ few m at $\gamma \sim 100$)

(2b) Hyperon decays may exhibit parity violation.

(3) Hyperons can be produced polarized !

Investigate: production, static properties, interactions, decays, etc.

Hyperon99 - Historical Overview

V J Smith, University of Bristol

- **Rochester & Butler (Manchester): V particles (1947)**

- **History of hyperon beams: CERN PS, Brookhaven AGS (1970's)**
  "Hyperon Beam Physics", J.Lach & L.Pondrom:
  Ann Rev Nucl Part Sci 29, 203-242 (1979)

- **Fermilab Neutral Hyperon Beam:** *ibid &*
  "Hyperon Experiments at Fermilab", L.G.Pondrom:
  Physics Reports 122, 57-172 (1985)

Fermilab Neutral Hyperon Beam

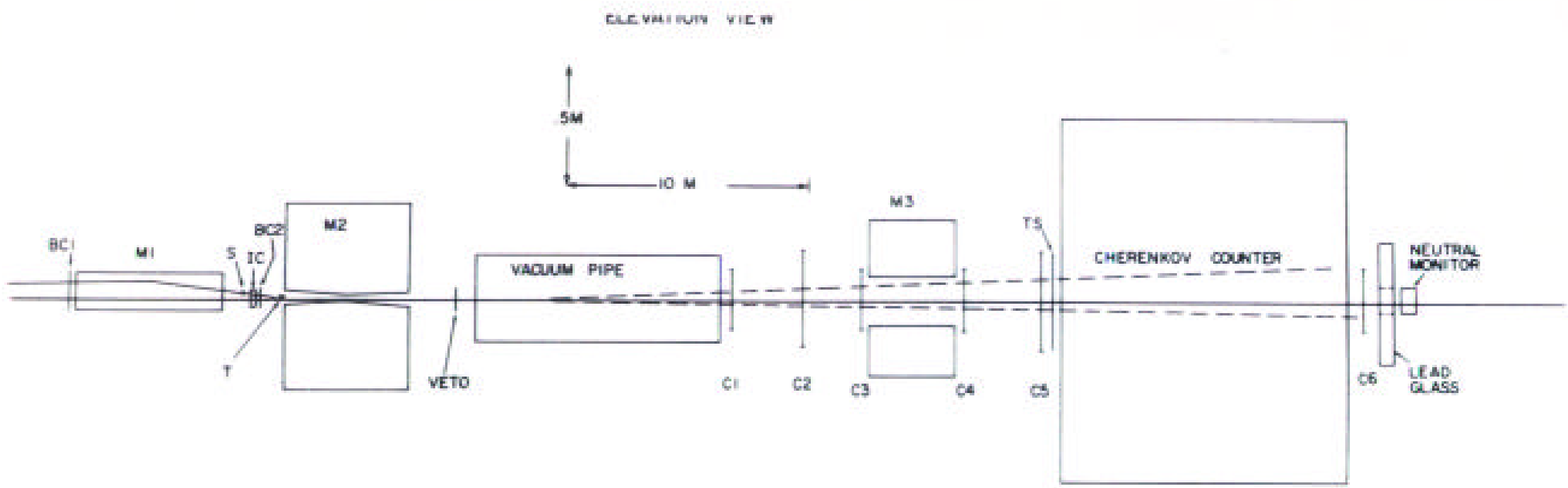

Figure 8 Layout of the Fermilab neutral hyperon beam. The magnet M1 restored the proton beam to the production target T. M2 was the neutral beam collimator and charged-particle sweeping magnet. Decays were observed after the veto by MWPCs C1–C6 and the analyzing magnet M3.

Fermilab Neutral Hyperon Beam

“. . . A series of experiments performed in a short neutral/charged beam in the Meson Laboratory at Fermilab. The first measurements were production cross-sections for 300 GeV protons; $p+Be \rightarrow \Lambda$, Λbar, K^0_S at secondary momenta between 60 and 250 GeV/c and fixed laboratory angles between 0 and 10 mrad.

At the larger production angles the Λ were polarized: $\langle P_\Lambda \rangle \sim 0.15$. The proton energy increased to 400 GeV. The Λ magnetic dipole moment was obtained: $\mu_\Lambda = (-0.6138 \pm 0.0047)\mu_N$. Production and polarization of Λbar, Ξ^0, Ξ^0bar, Σ^+, Σ^-, and Ξ^- were studied in roughly the same kinematic range as the Λ.

The A dependence of the cross-sections from Be, Cu, Pb targets was measured, and production cross-sections $pp \rightarrow \Lambda$, Λbar, K^0_S from a liquid hydrogen target were obtained.

Fermilab Neutral Hyperon Beam

The magnetic moments $\mu_{\Xi 0}$=(-1.253 ± 0.014)μ_N, $\mu_{\Xi-}$= (-0.69 ± 0.04)μ_N, $\mu_{\Sigma+}$=(+2.31 ± 0.03)μ_N, and $\mu_{\Sigma-}$=(-0.89 ± 0.14) resulted from further work with the precession of polarized hyperons.

Although the production cross-sections and polarizations are considered from the triple-Regge point of view, the main theme of the report is the constituent quark model, which, combined with some ancillary assumptions gives a better than qualitative picture of all of these phenomena."

Fermilab Charged Hyperon Beam: E-497

210 GeV/c secondary beam.

+ve beam: 0.5% Σ^+ Pol ~ 0.2 $\quad \mu_{\Sigma+} = (2.38 \pm 0.02)\mu_N$

-ve beam: 20% Σ^- Pol ~ 0.2 $\quad \mu_{\Sigma-} = (-1.23 \pm 0.03 \pm 0.03)\mu_N$

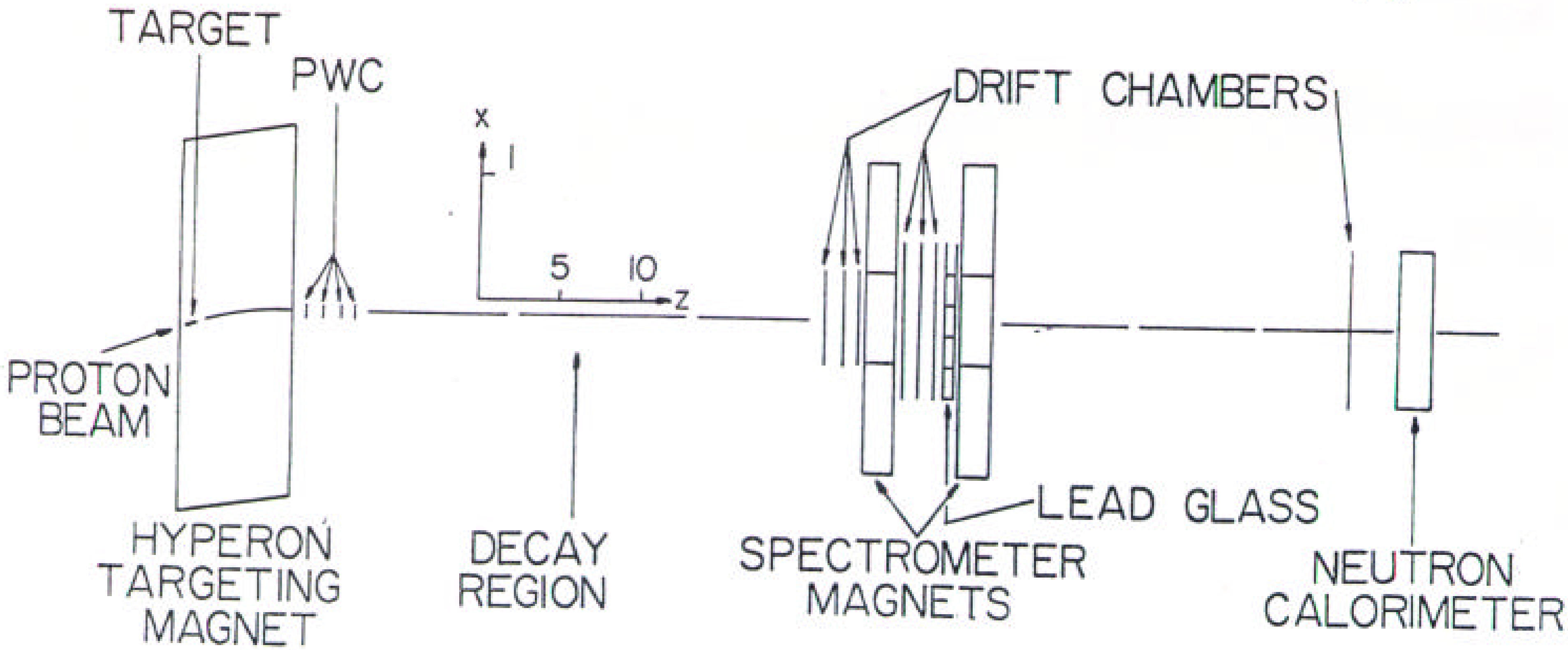

Outline of talk:

1. First SPS charged hyperon beam: Y1

Beam description;

Experiments WA2, WA46, WA42, WA62;

Physics Results.

2. Second SPS charged hyperon beam: Y2

Beam description;

Experiment WA89;

Physics Results.

CERN West Hall

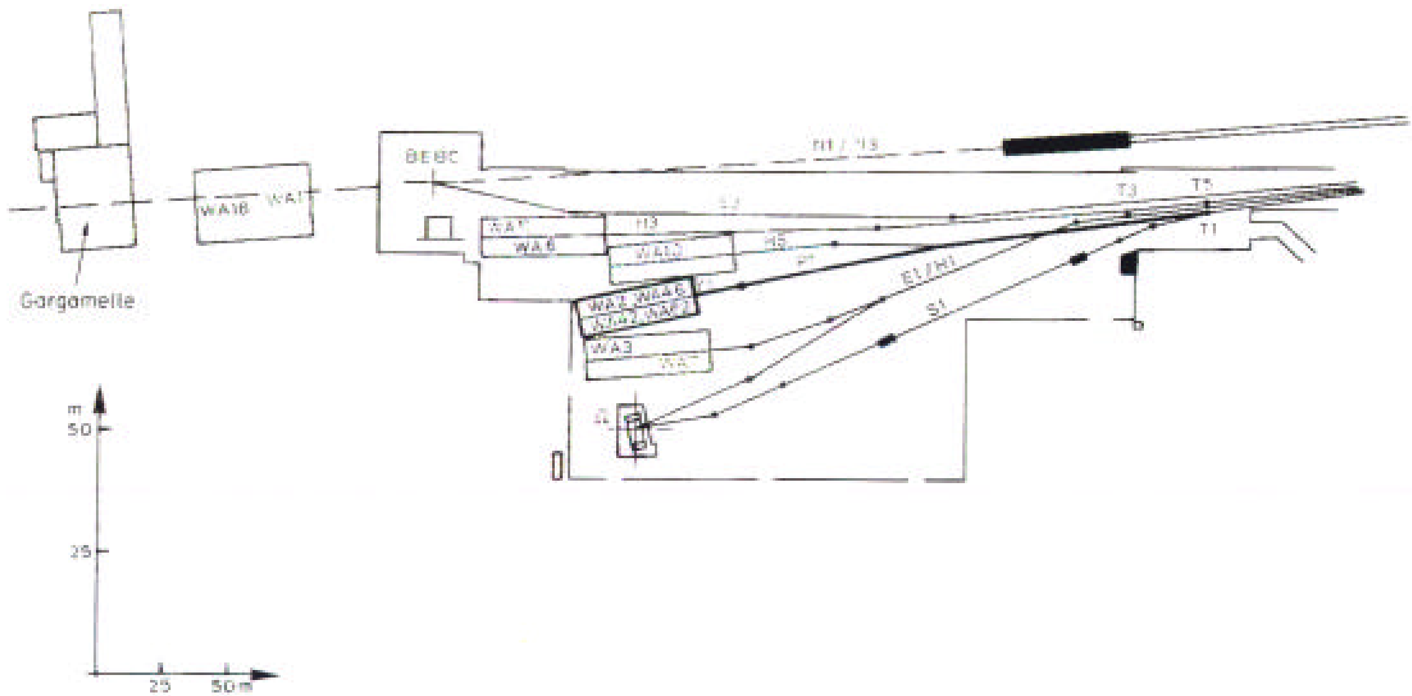

Fig. 3.2. General layout of the SPS West Experimental Area (1976–1982). P1 refers to the line transporting protons to the Y1 hyperon production target

SPS hyperon beam Y1 (1976-1982)

Ref: Bourquin & Repellin, Physics Reports 114 (1984) 99-180

Beam Description:

Table 3.1
Comparison of typical parameters and hyperon fluxes between the PS and SPS charged hyperon beams

	PS beam	SPS beam
Proton momentum	24 GeV/c	200 GeV/c
Hyperon momentum	17 GeV/c	130 GeV/c
Channel length	4.2 m	12.6 m
Σ^-/π^- at production	0.8	0.6
Σ^- decay factor	780	14.6
Σ^-/π^- at channel exit	10^{-3}	4×10^{-2}
Ω^-/π^- at production	5×10^{-4} (assumed)	5×10^{-4}
Ω^- decay factor	1.5×10^{7}	6.5×10^{2}
Ω^-/π^- at channel exit	3.3×10^{-11}	7.7×10^{-7}

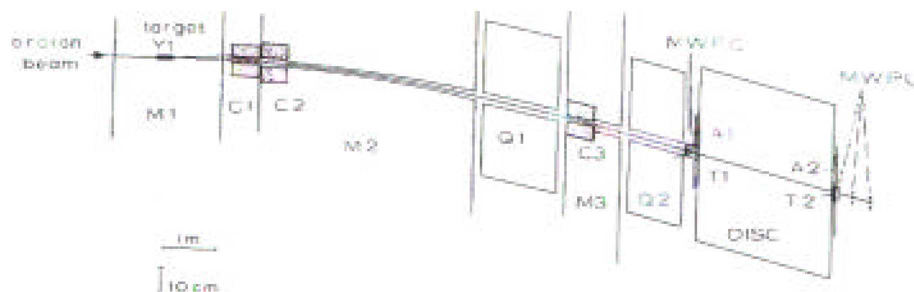

Fig. 3.1. Schematic representation of the SPS charged hyperon beam. M1, M2, M3 are bending magnets; Q1 and Q2 are superconducting quadrupoles; C1, C2, C3 are horizontally adjustable collimators. The location of the DISC counter is also shown.

SPS DISC

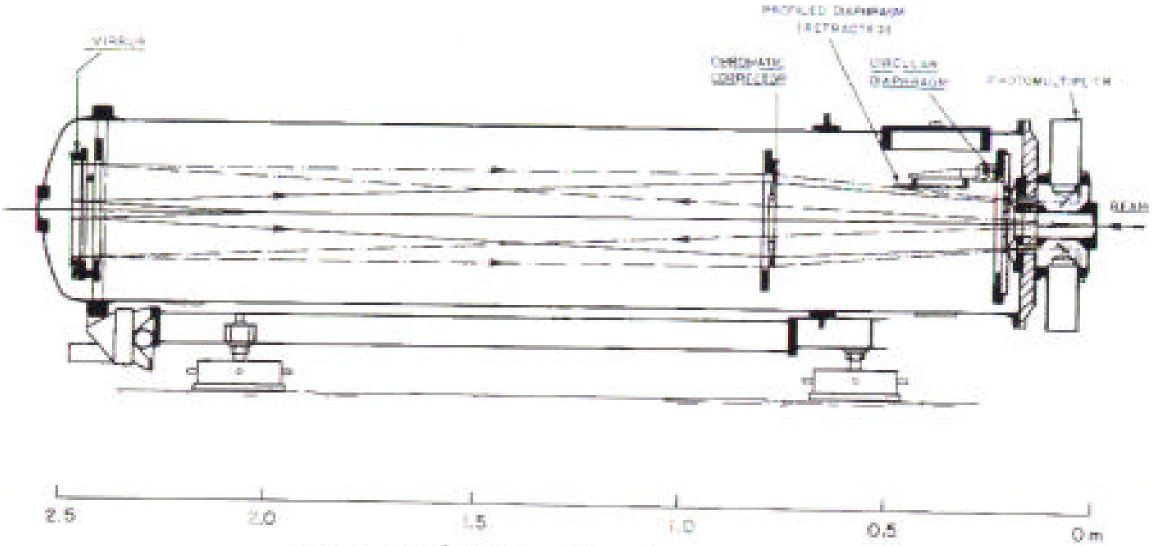

Fig. 3.3. The DISC Čerenkov counter of

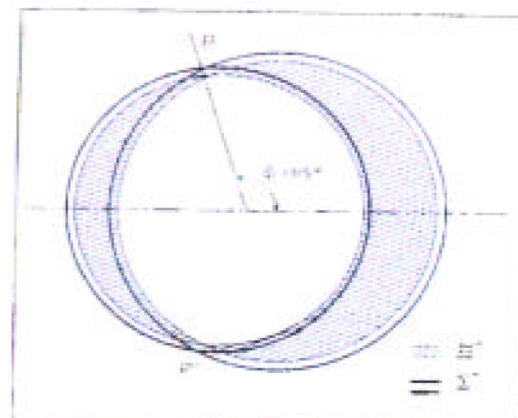

Fig. 3.5. Schematic representation of the envelopes of the Σ^- and Ξ^- Čerenkov ring images in the plane of the DISC diaphragm

DISC Scans

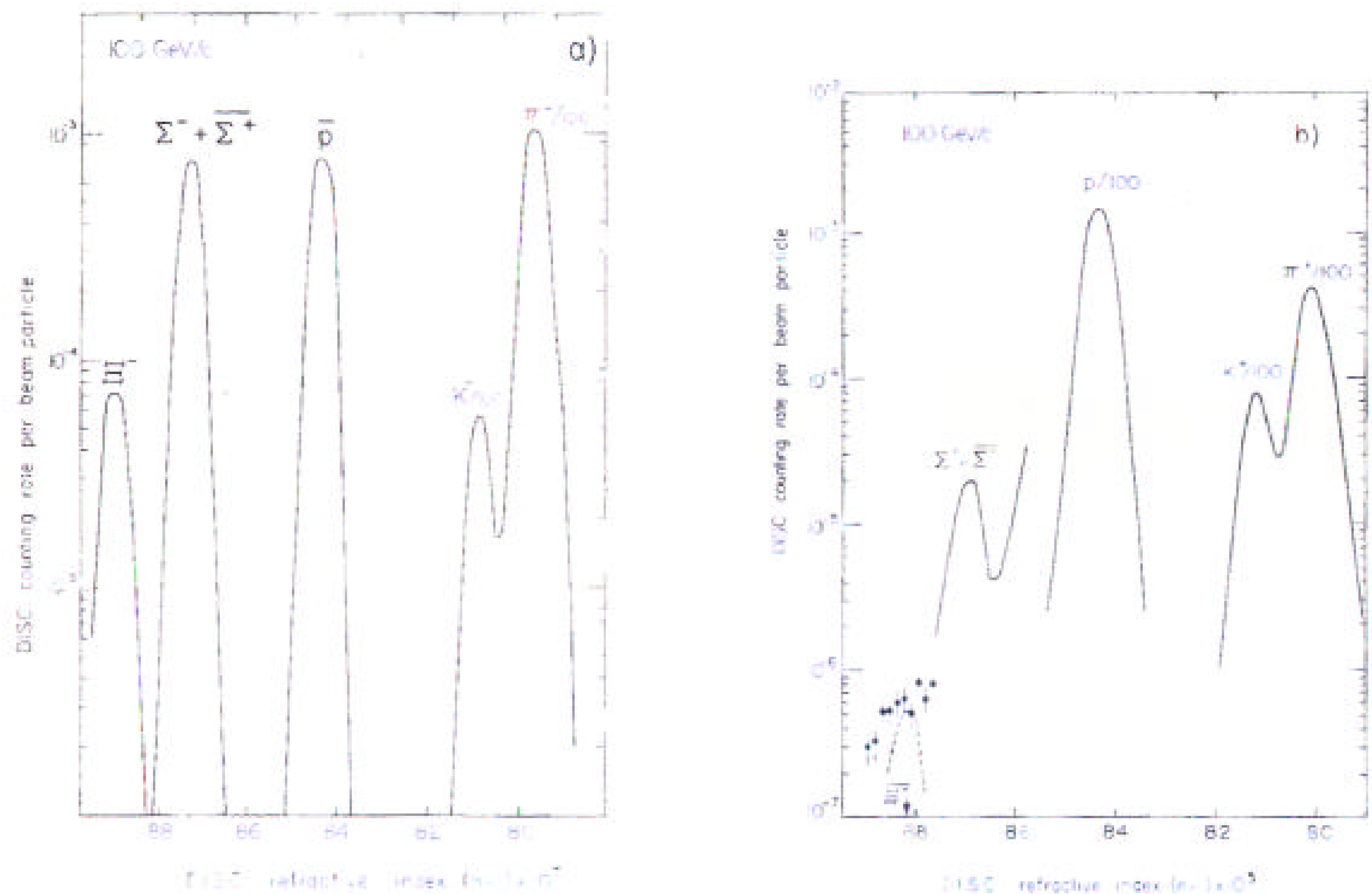

Fig. 7.1. DISC counting rate as a function of the refractive index, with the beam set at 100 GeV/c. a) Negative polarity (diaphragm opening [illegible] mrad). b) Positive polarity (diaphragm opening [illegible] mrad).

WA2 Apparatus

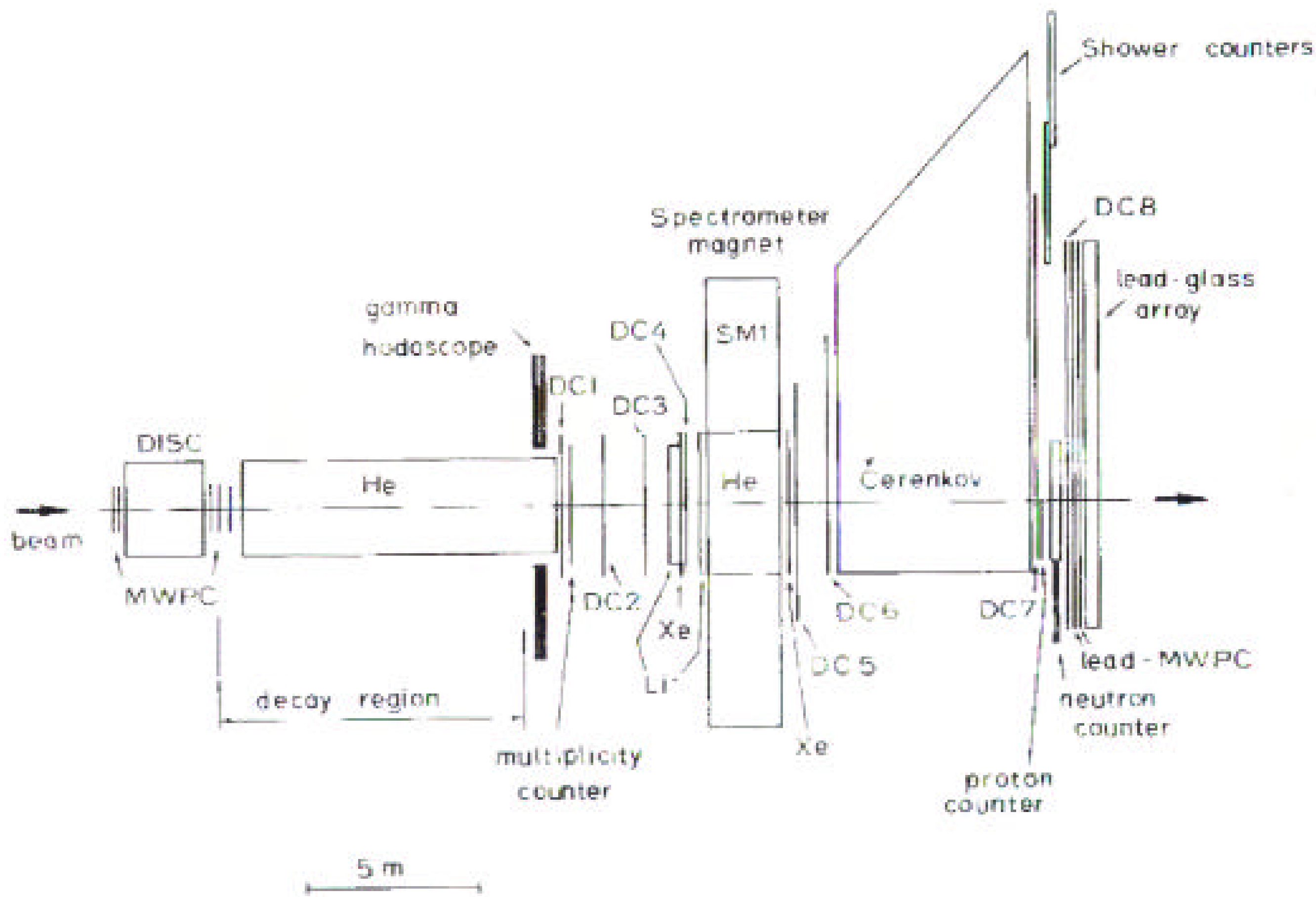

Fig. 4.1. Layout of the spectrometer and electron/photon detectors in the first apparatus installed in the SPS hyperon beam. DC1 to DC8 are chambers. Li and Xe are the radiators and the proportional chambers of the transition radiation detectors.

Hyperon mass peaks

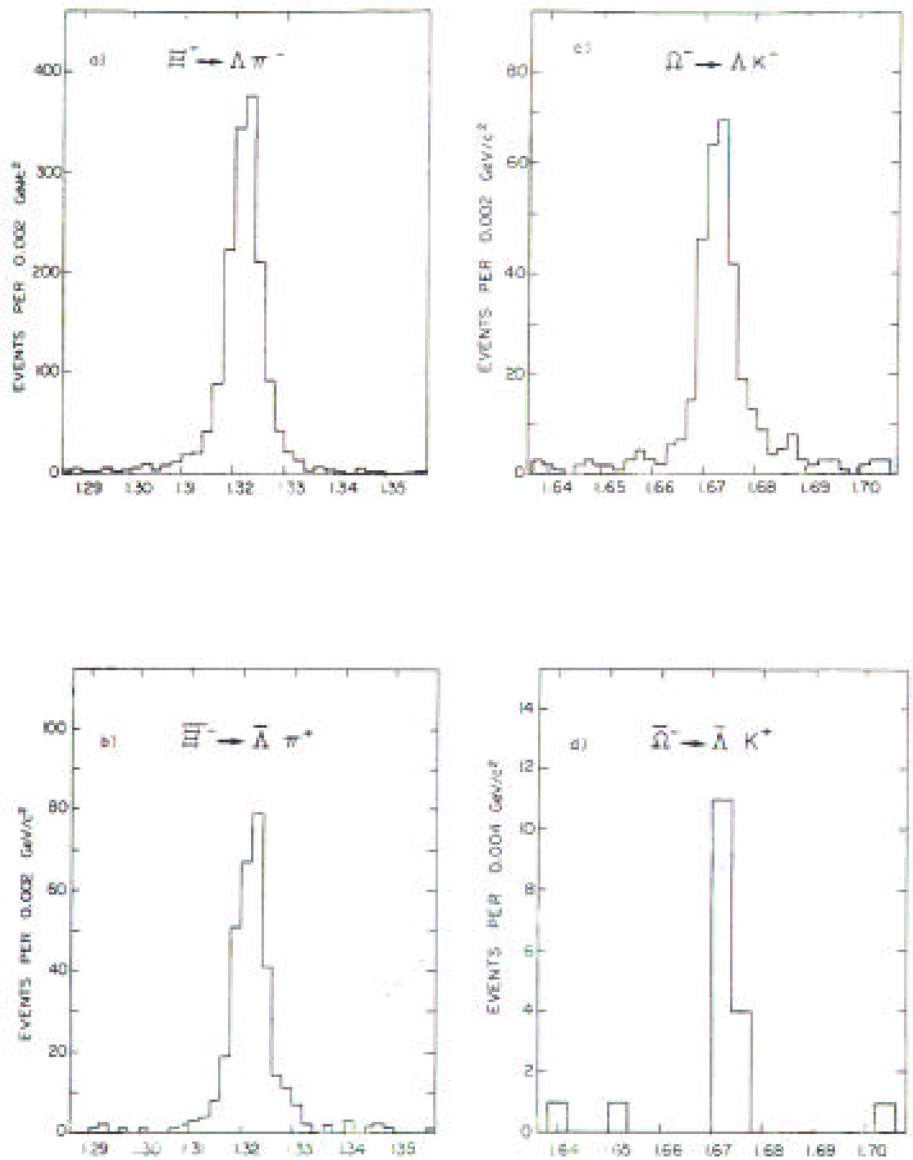

Fig. 3.1 The (Λπ) and (ΛK) effective masses (GeV/c²): a) $\Xi^- \rightarrow \Lambda\pi^-$; b) $\overline{\Xi}^- \rightarrow \overline{\Lambda}\pi^+$; c) $\Omega^- \rightarrow \Lambda K^-$; d) $\overline{\Omega}^- \rightarrow \overline{\Lambda}K^+$.

Table 3.2

The number of hyperons identified by the DISC for 10^6 secondary beam particles. These numbers are indicative only as they depend upon the specific requirements of each experiment

Proton beam momentum (GeV/c)	200	250
Hyperon momentum (GeV/c)	100	135
Σ^-	4000	15 000
Σ^+	46	100
$\overline{\Sigma}^-$	6	
$\overline{\Sigma}^+$	2	
Ξ^-	400	
$\overline{\Xi}^-$		2
Ω^-	0.2	1.3

Particle yields

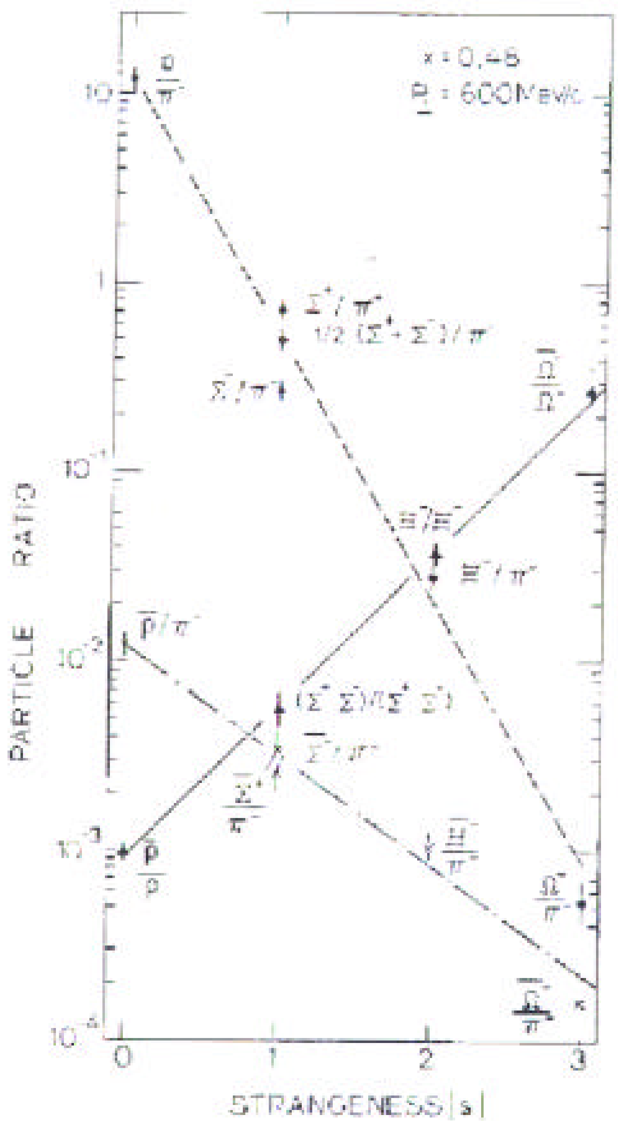

tion of the baryon or antibaryon strangeness at $x = 0.46$ and $p_T = 600$ MeV/c

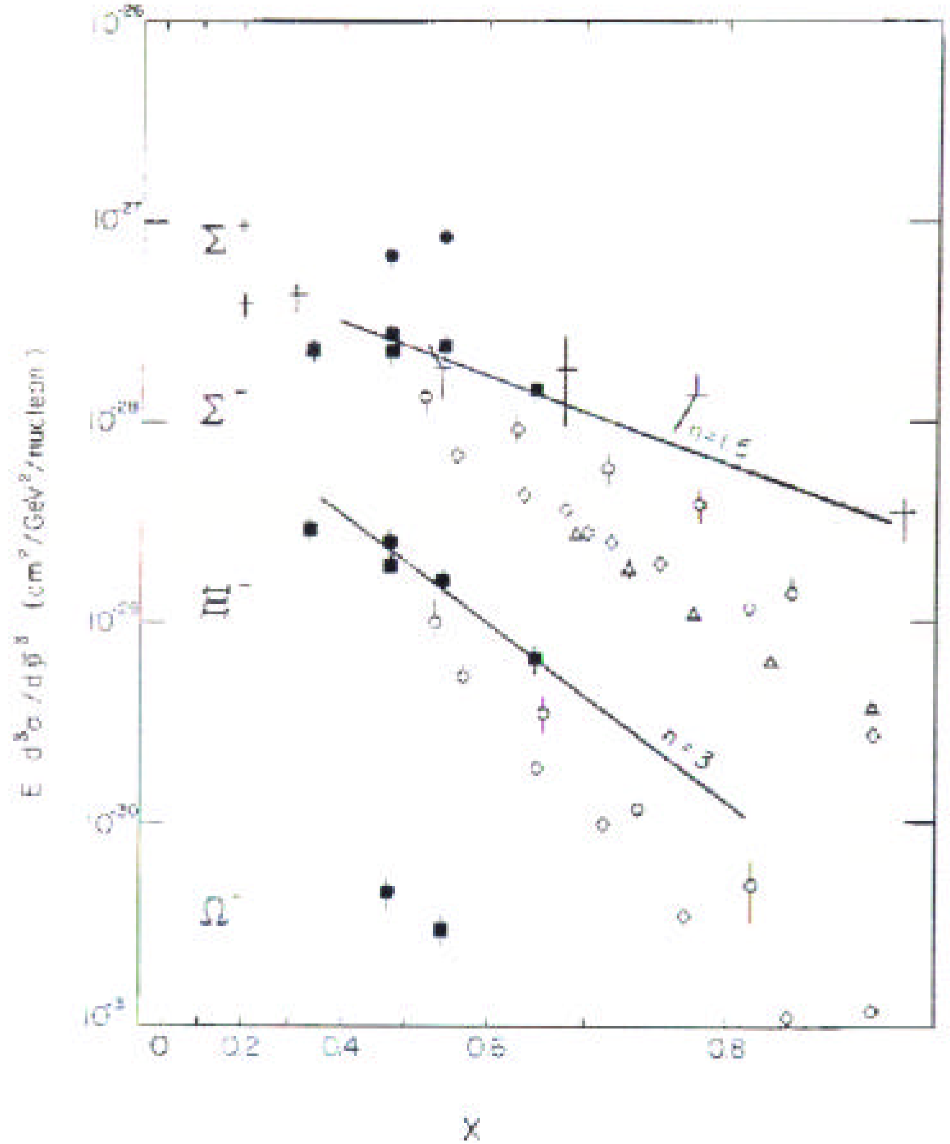

variant inclusive hyperon cross-section as a function of x for p_T close to zero: ●■ SPS hyperon beam

WA2 Hyperon Semi-leptonic Decays

SL branching ratios 10^{-3} - 10^{-5}

$\rightarrow$ large hadronic background.

Excellent electron identification is essential.

WA2 had 4 electron detectors:

2 TRD (one magnet-assisted); lead glass;

threshold Cerenkov; lead-scint shower counter.

(TRD: Li foil radiator + sealed Xe/CO_2 chambers.)

Independent detectors: allows cross-calibration;

overall rejection is nearly multiplicative;

eg 45:1 for TRD * 1000:1 for lead-glass => 40,000:1

Lead glass detector

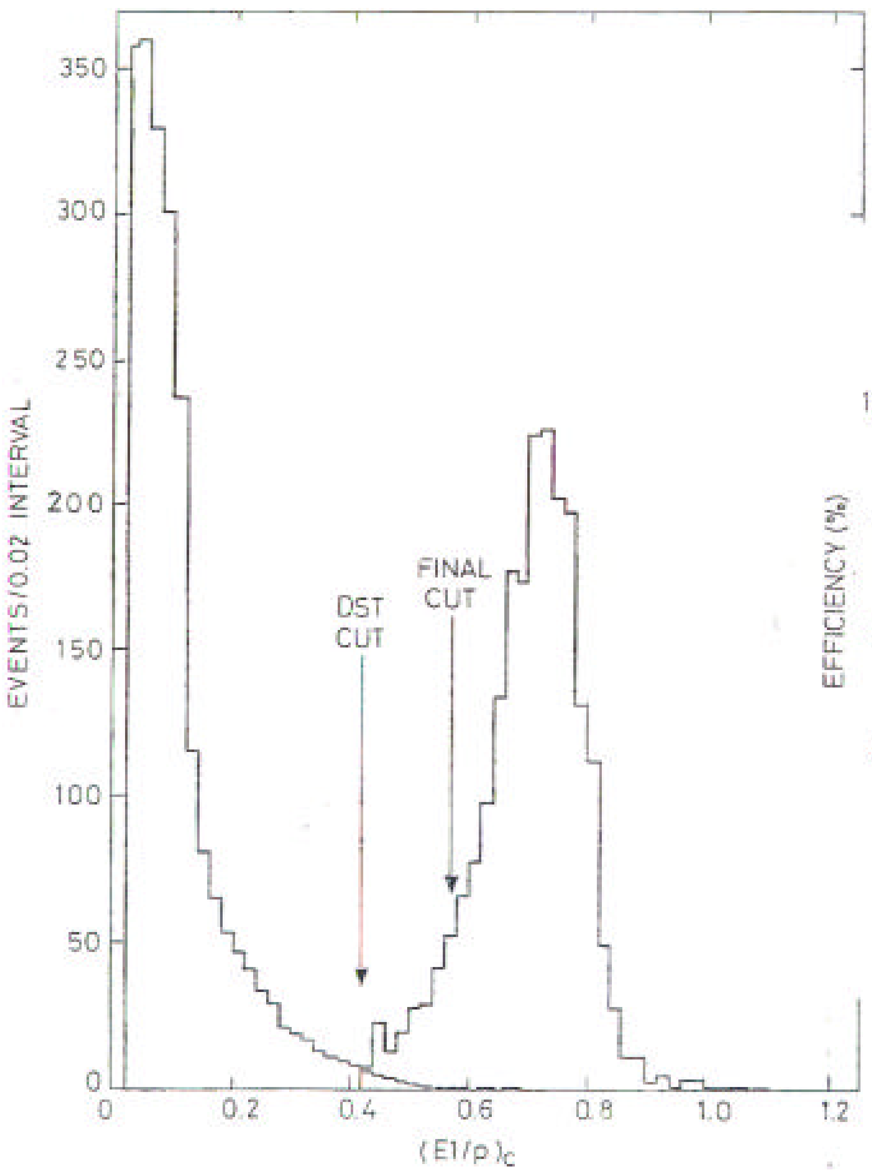

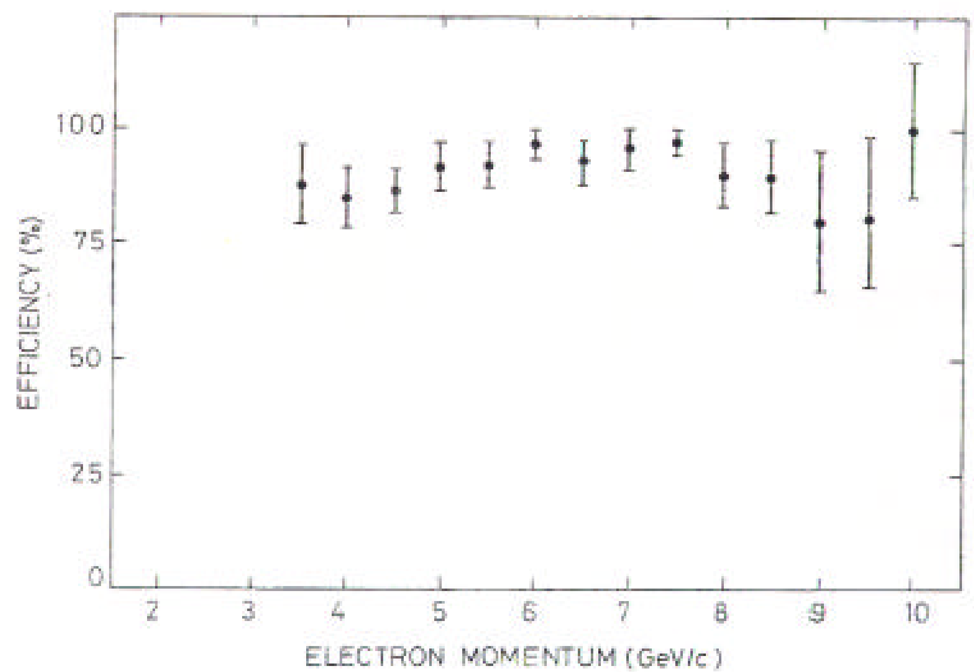

WA2 Hyperon Semi-leptonic Decays

decay	Cabibbo angle	V coeff. (g_V or f_1)	A coeff. (g_A or g_1)	g_A/g_V (g_1/f_1)
$n \to p e \nu$	$\cos\theta_c$	1	$F+D$	$F+D = 1.25$
$\Lambda \to p$	$\sin\theta_c$	$-\sqrt{\frac{3}{2}}$	$-\sqrt{\frac{3}{2}}(F+\frac{D}{3})$	$F+D/3$
$\Sigma^- \to n$	$\sin\theta_c$	-1	$-F+D$	$F-D$
$\Sigma^- \to \Lambda$	$\cos\theta_c$	0	$\sqrt{\frac{2}{3}}D$	—
$\Xi^- \to \Lambda$	$\sin\theta_c$	$\sqrt{3/2}$	$\sqrt{\frac{3}{2}}(F-\frac{D}{3})$	$F-D/3$
$\Xi^- \to \Sigma^0$	$\sin\theta_c$	$\frac{1}{\sqrt{2}}$	$\frac{1}{\sqrt{2}}(F+D)$	$F+D$

WA2

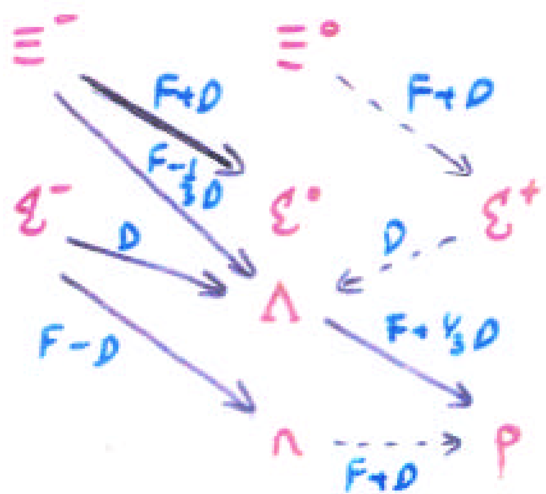

Table 6.2
WA2 event samples

Decay	Final sample	Background contamination
$\Sigma^- \to ne^-\bar{\nu}$	4456	370
$\Sigma^- \to \Lambda e^-\bar{\nu}$	1649	3
$\Lambda \to pe^-\bar{\nu}$	7802	690
$\Xi^- \to \Lambda e^-\bar{\nu}$	2582	590
$\Xi^- \to \Sigma^0 e^-\bar{\nu}$	305	151

Table 6.3
WA2 branching ratios and form factor ratios

Decay	Branching ratio [$\times 10^{-4}$]	$g_1(0)/f_1(0)$
$\Sigma^- \to ne^-\bar{\nu}$	9.6 ± 0.5	-0.34 ± 0.05
$\Sigma^- \to \Lambda e^-\bar{\nu}$	0.56 ± 0.03	$+0.03 \pm 0.08$*)
$\Lambda \to pe^-\bar{\nu}$	8.57 ± 0.36	$+0.70 \pm 0.03$
$\Xi^- \to \Lambda e^-\bar{\nu}$	5.64 ± 0.31	$+0.25 \pm 0.05$
$\Xi^- \to \Sigma^0 e^-\bar{\nu}$	0.87 ± 0.17	

*) $f_1(0)/g_1(0)$ is quoted in this case.

Semileptonic decay results

Since many years the branching ratios and form factor measurements of the semileptonic hyperon decays have been used in global fits of the Cabibbo model. These fits were made by combining results from many different experiments often with poor statistics [41].

With the completion of the WA2 experiment the experimental situation has significantly improved. Using these new results various fits were performed [42], which are particularly reliable since they combine all the measurements on the five decays with large statistics, a coherent treatment of the q^2 dependence and of the internal radiative corrections. As an example a fit using all the WA2 results, the G value determined from the muon lifetime and the most recent compilation of the neutron lifetime [43] gives the following values:

$$F = 0.477 \pm 0.012$$
$$D = 0.756 \pm 0.011$$
$$\sin\theta_c = 0.231 \pm 0.003 .$$

The result of this fit is shown in fig. 6.9. Each decay constrains the allowed values of F and D to lie in a band in the FD plane, the orientations of which depend on the decay as shown in table 6.1. The limits

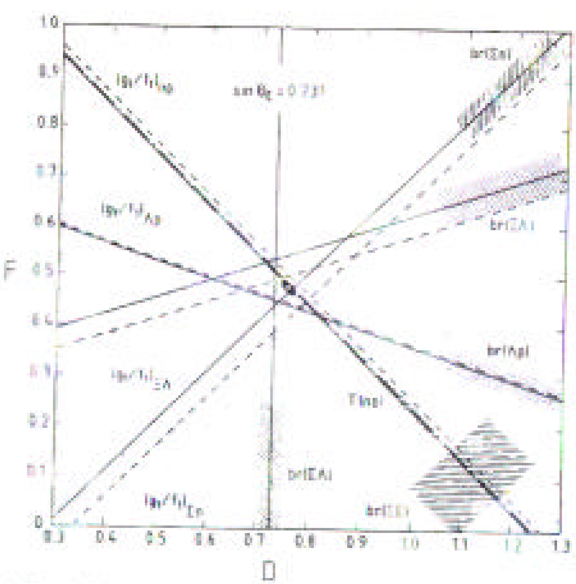

Fig. 6.9. Result of the Cabibbo fit in the FD plane. Full and dotted lines correspond to the branching ratios and form factor ratio constraints, respectively.

Experiment WA46: Ω^- decays

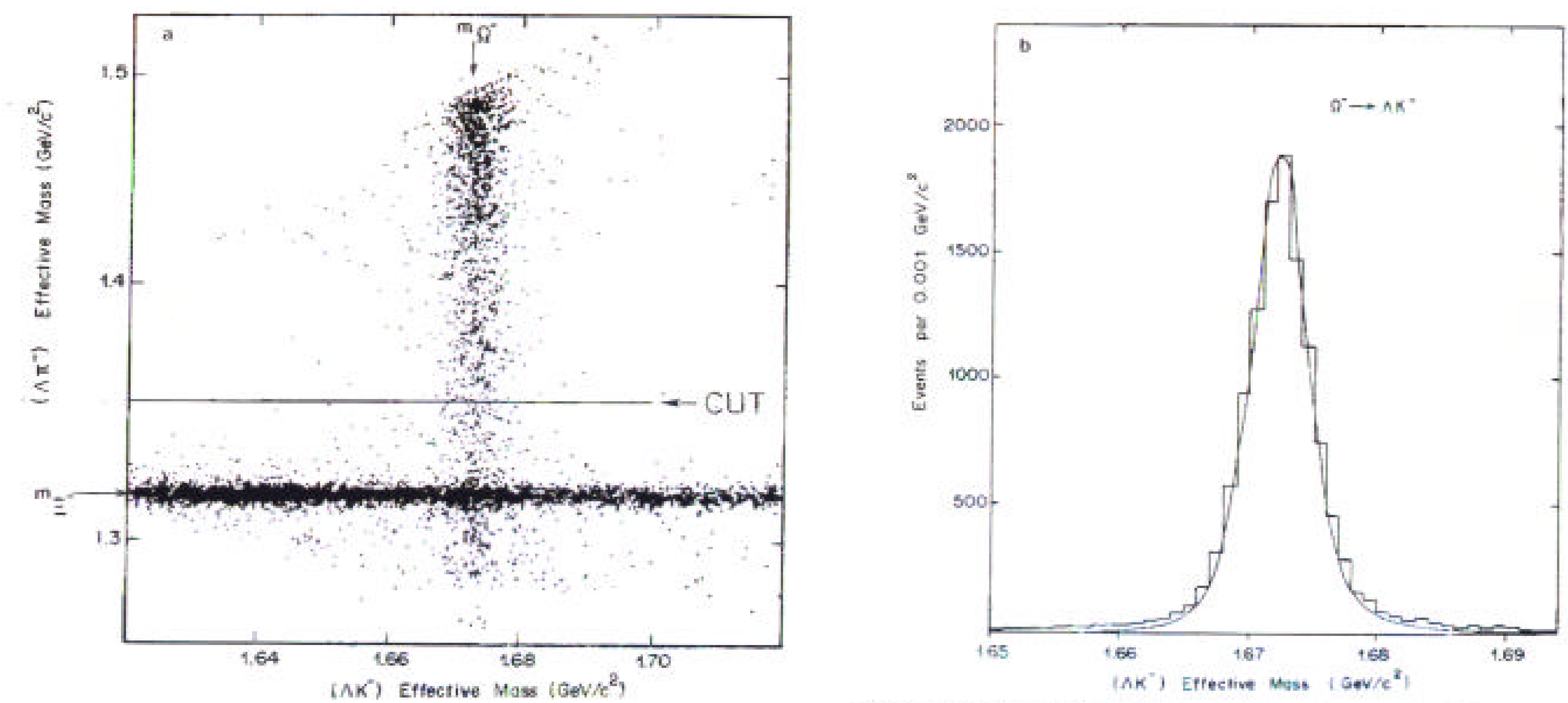

andidates: a) $(\Lambda\pi^-)$ versus (ΛK^-) effective mass combinations for a partial sample. The line represent nass after applying the cut.

Experiment WA46: Ω^- decays

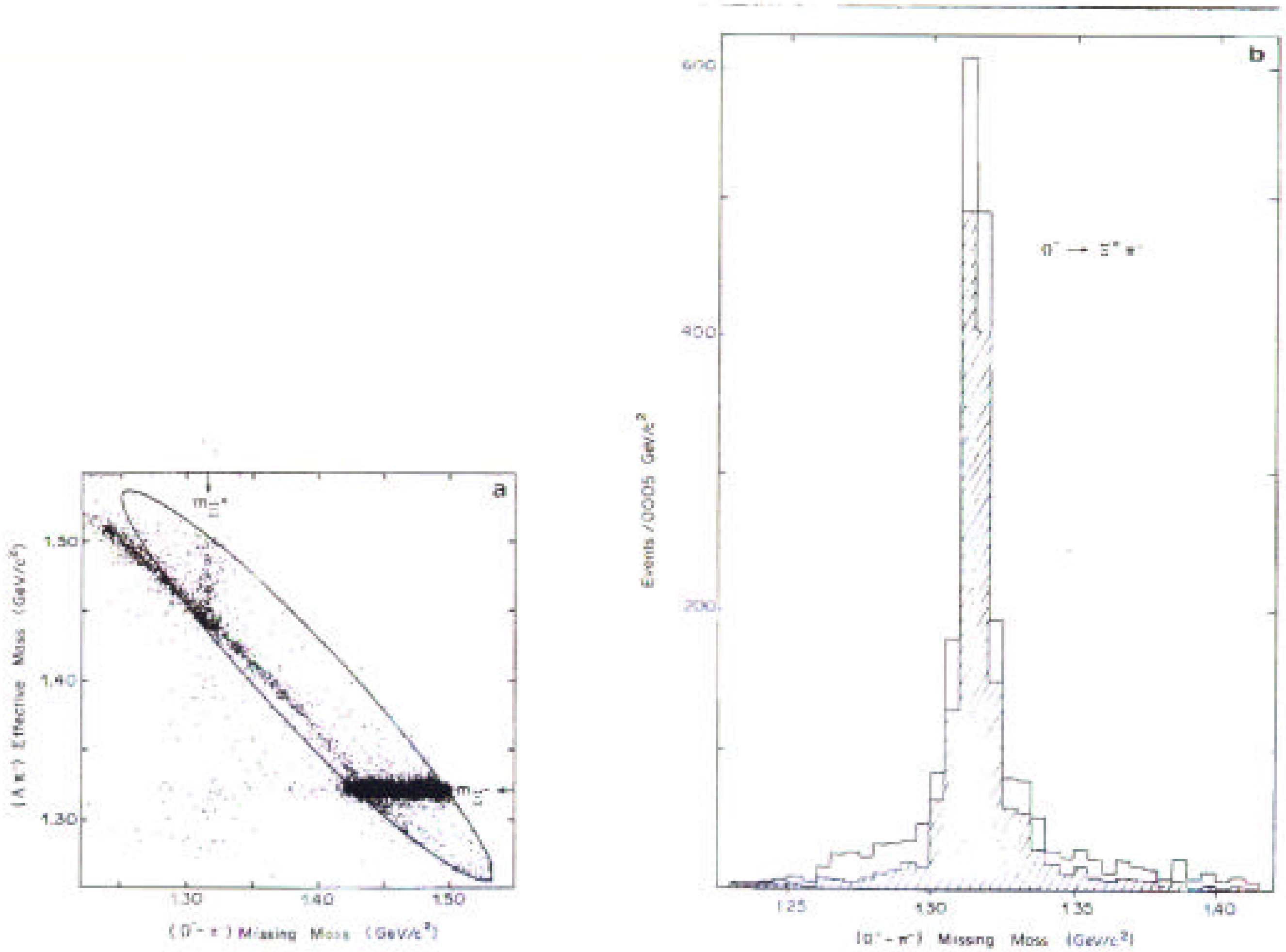

Fig 7.2. The $\Omega^- \to \Xi^0\pi^-$ candidates: a) The $(\Lambda\pi^-)$ effective mass versus $(\Omega^- - \pi^-)$ missing mass for a partial sample. The kinematical boundaries of the $(\Lambda\pi^-\pi^0)$ final state for Ω is indicated by the line. b) The $(\Omega^- - \pi^-)$ missing mass after applying a cut on the $(\Lambda\pi)$ mass and on the missing longitudinal momentum.

Experiment WA46: Ω^- decays

Lifetime results:

$\tau = (0.823 \pm 0.013) \times 10^{-10}$ s for $\Omega^- \to \Lambda K^-$

$\tau = (0.82 \pm 0.05) \times 10^{-10}$ s for $\Omega^- \to \Xi^0 \pi^-$

$\tau = (0.92 \pm 0.07) \times 10^{-10}$ s for $\Omega^- \to \Xi^- \pi^0$

Branching ratio results:

$BR(\Omega^- \to \Lambda K^-) = 0.678 \pm 0.007$

$BR(\Omega^- \to \Xi^0 \pi^-) = 0.236 \pm 0.007$

$BR(\Omega^- \to \Xi^- \pi^0) = 0.086 \pm 0.004$

(inconsistent with $\Delta I = \frac{1}{2}$ rule by 4 sd)

Experiments WA42, WA62

Σ^-, Ξ^- total cross-sections on p and d;

Ξ^- - p elastic cross-sections; $\Xi^- \not\to n\pi^-$;

Ξ^* resonances; $\Xi^- \to \Lambda\pi^-$ α–parameter;

$\Xi_c^+ \to \Lambda K^-\pi^+\pi^+$ observation and lifetime;

Ω_c^0 (3 events!); U(3100) (?);

WA42 apparatus

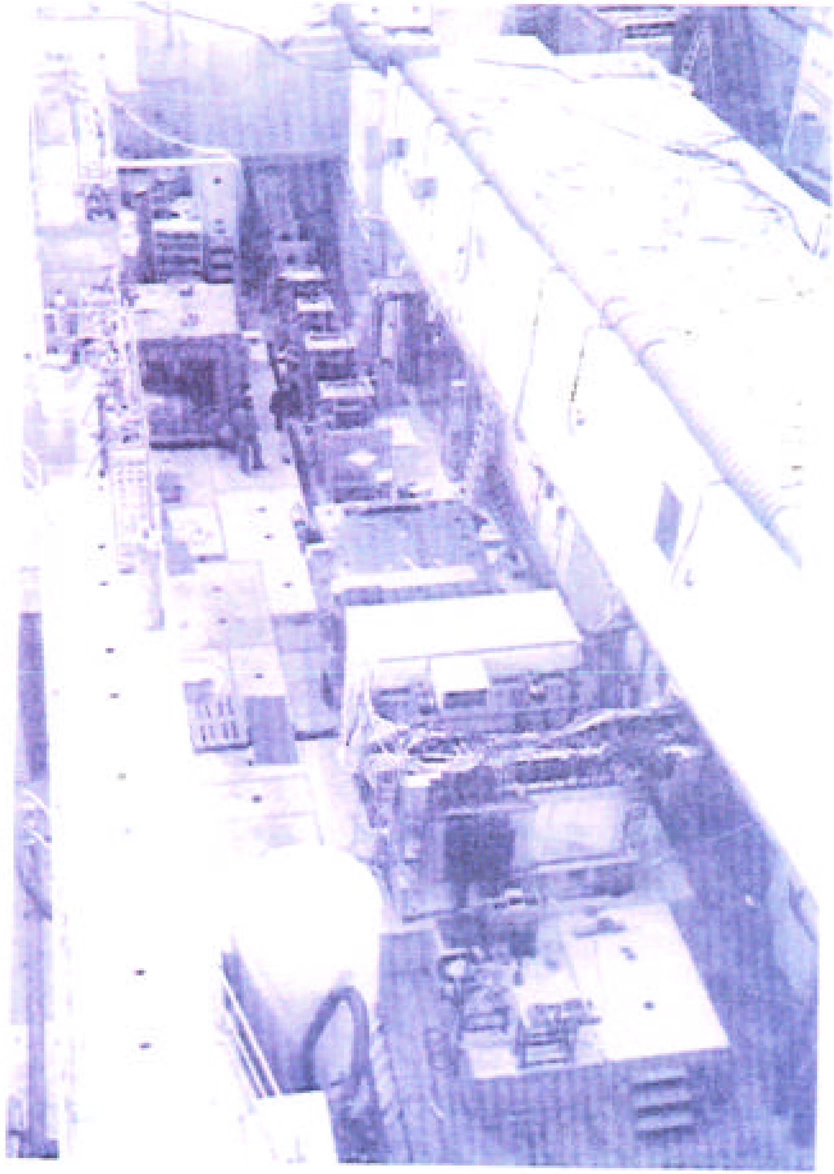

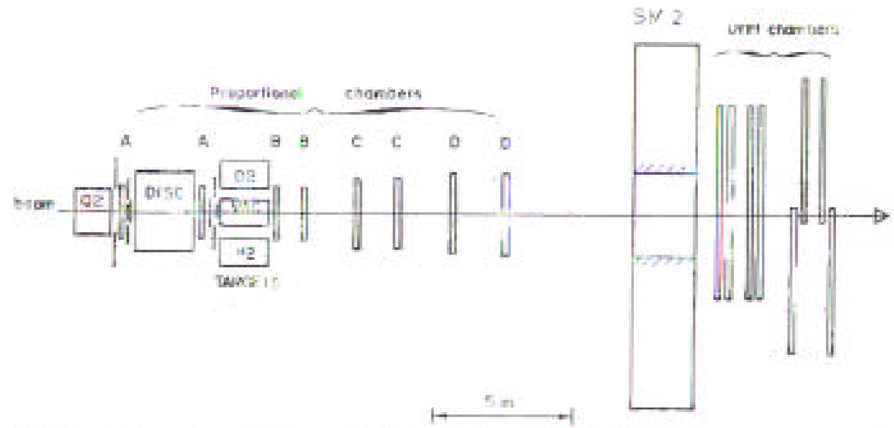

Fig. 6.1. A schematic plan view of the [illegible] apparatus installed in the SPS hyperon beam. A,B,C and D [illegible] groups of proportional chambe

WA42 total cross-section measurement

Improved DISC efficiency, detects incoming Σ^- or Ξ^-;

scattered hyperon detected by decay π^-.

Measure transmission of hyperons in liquid hydrogen, liquid deuterium, empty target.

No acceptance correction required.

Σ^- measurements at 75, 86, 101, 120, 137 GeV/c;

Ξ^- measurements at 102, 134 GeV/c.

WA42 total cross-section measurement

M. Bourquin and J.-P. Repellin, Experiments with the CERN SPS hyperon beam

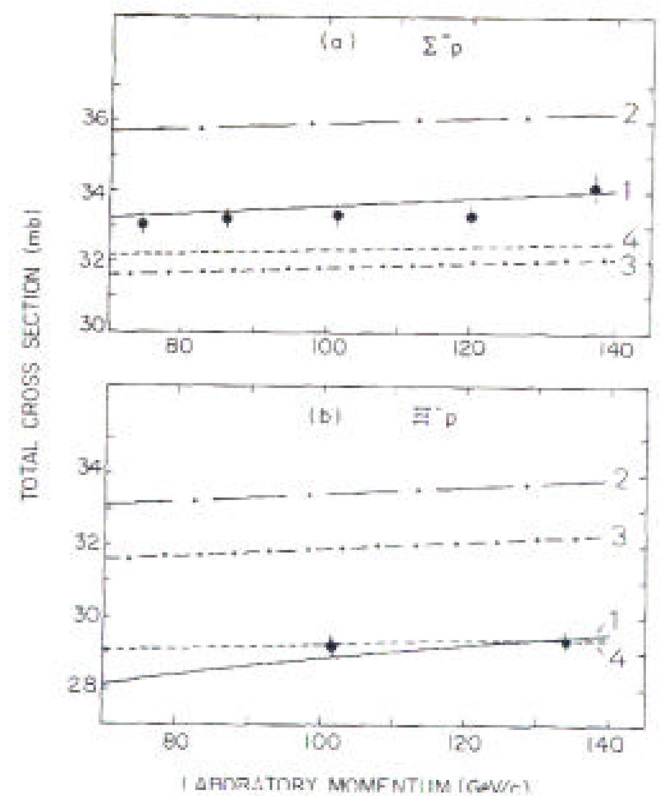

WA42 : Ξ^- properties

Using spectrometer to reconstruct Ξ^-:

α parameter for $\Xi^- \to \Lambda\pi-$

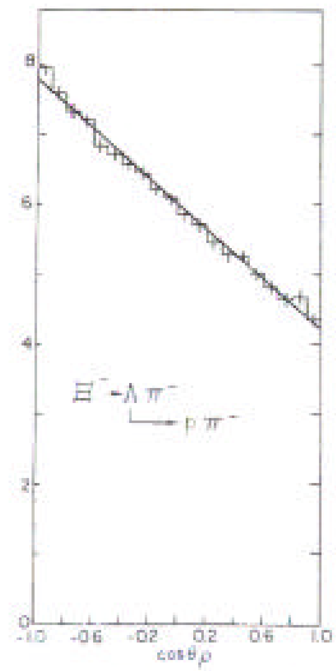

Fig. [illegible]. Proton angular distribution in the Λ centre-of-mass for $\Xi^- \to \Lambda\pi^-$, $\Lambda \to p\pi^-$. The histogram contains [illegible] events. The straight line is the result of the least squares fit.

WA42 : Ξ^- properties

Ξ^--proton elastic scattering

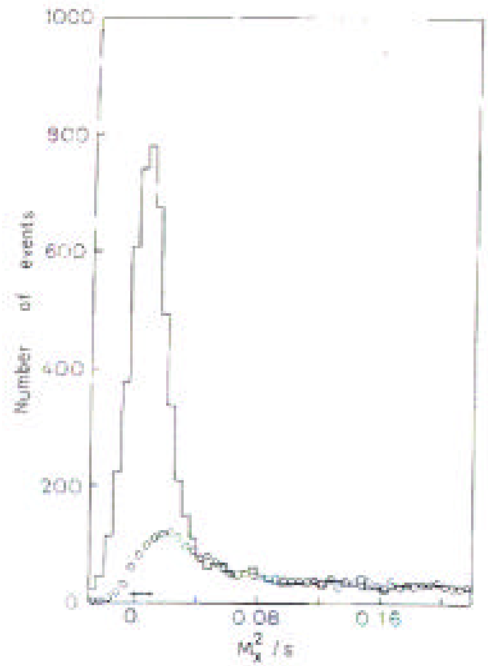

Fig. 11.2. The M_X^2/s distribution for the scattering process $\Xi^- p \to \Xi^- X$ at 102 GeV/c, with $0.08 < -t < 0.6$ (GeV/c)^2. Histogram: experimental sample; open circles: simulated inelastic events. The horizontal double arrow indicates the region of the proton peak used to obtain the elastic cross-section.

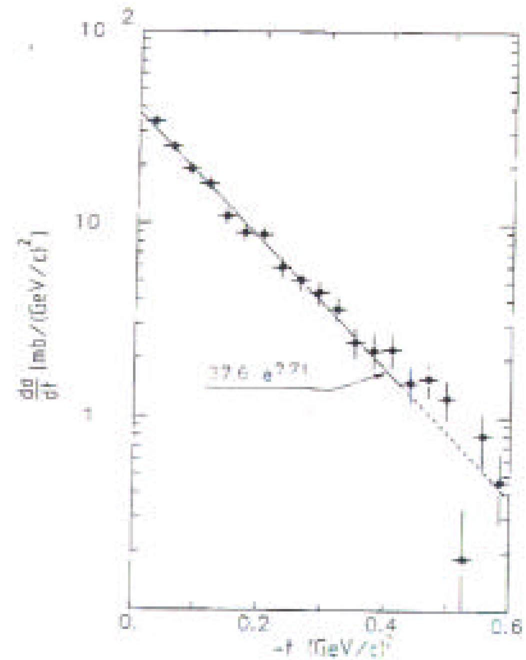

Fig. 11.3. The $\Xi^- p$ elastic differential cross-section at 102 GeV/c, as a function of the momentum transfer squared.

WA42 : Ξ^- properties

$\Xi^- \not\to n\pi^-$ $(\Delta S=2)$ **BR**$< 1.9 \times 10^{-5}$

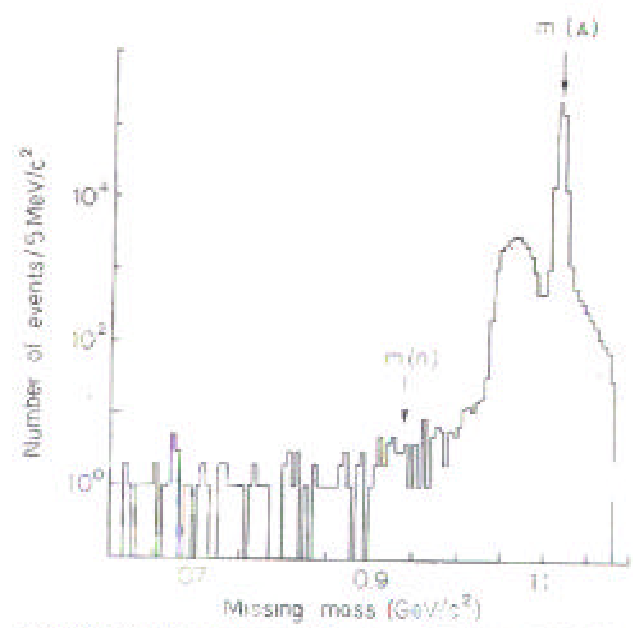

Fig. 10.2. Missing mass spectrum for the decays $\Xi^- \to X\pi^-$ at 102 GeV/c.

WA42 : Ξ^* resonances

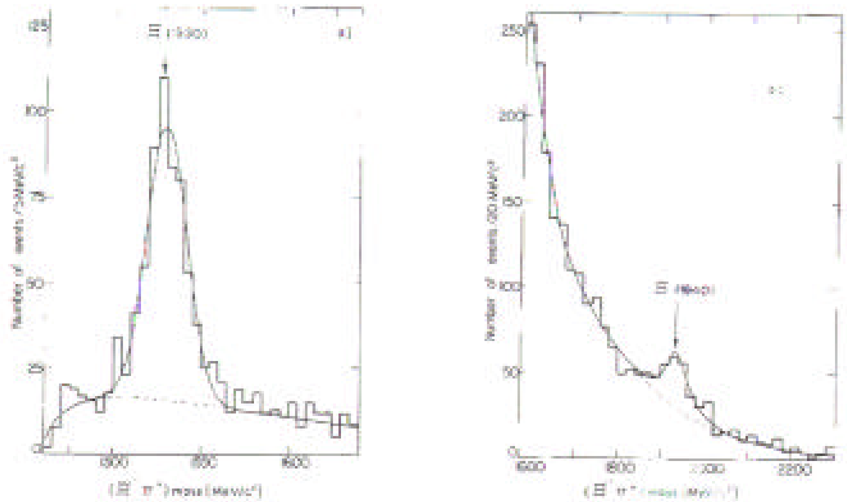

Fig. 11.4. The $(\Xi^- \pi^+)$ effective mass distributions: a) 135 GeV/c H_2 target data. b) 102 and 135 GeV/c data from H_2 and D_2 targets.

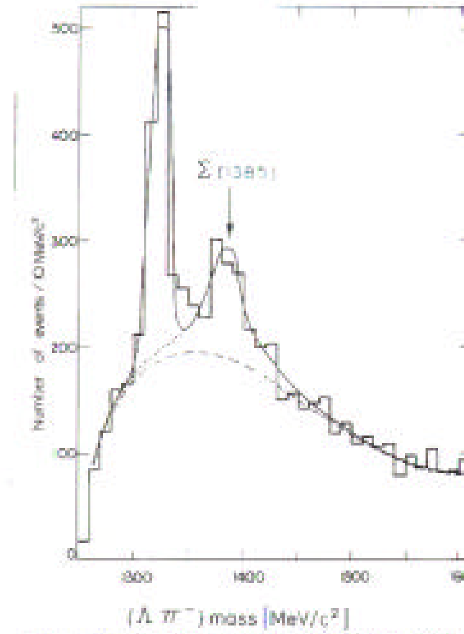

Fig. 11.5. The $(\Lambda \pi^-)$ effective mass distribution from the 135 GeV/c H_2 target data. The transmitted Ξ^- have been suppressed.

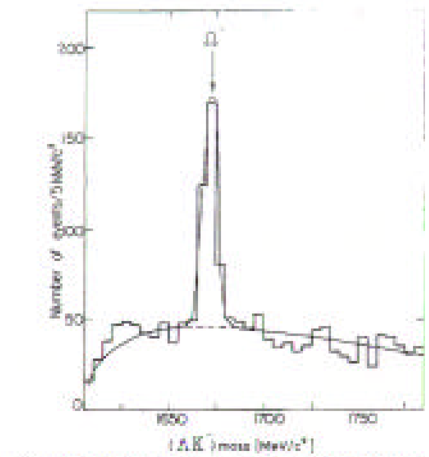

Fig. 11.6. The (ΛK^-) effective mass distribution from the 135 GeV/c H_2 target data.

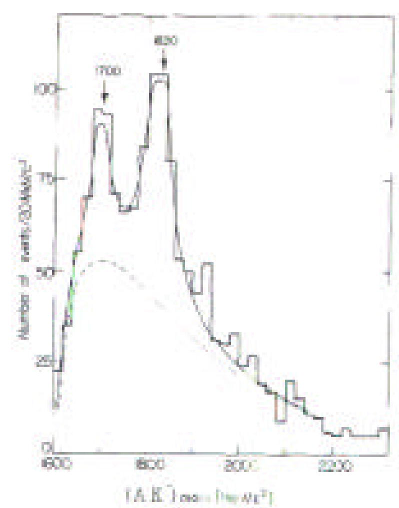

Fig. 11.7. The (ΛK^-) effective mass distribution from 102 and 135 GeV/c, H_2 and D_2 data. The events are required to be diffractive to suppress Ω production.

WA62: charm-strange baryons

Experimental apparatus:

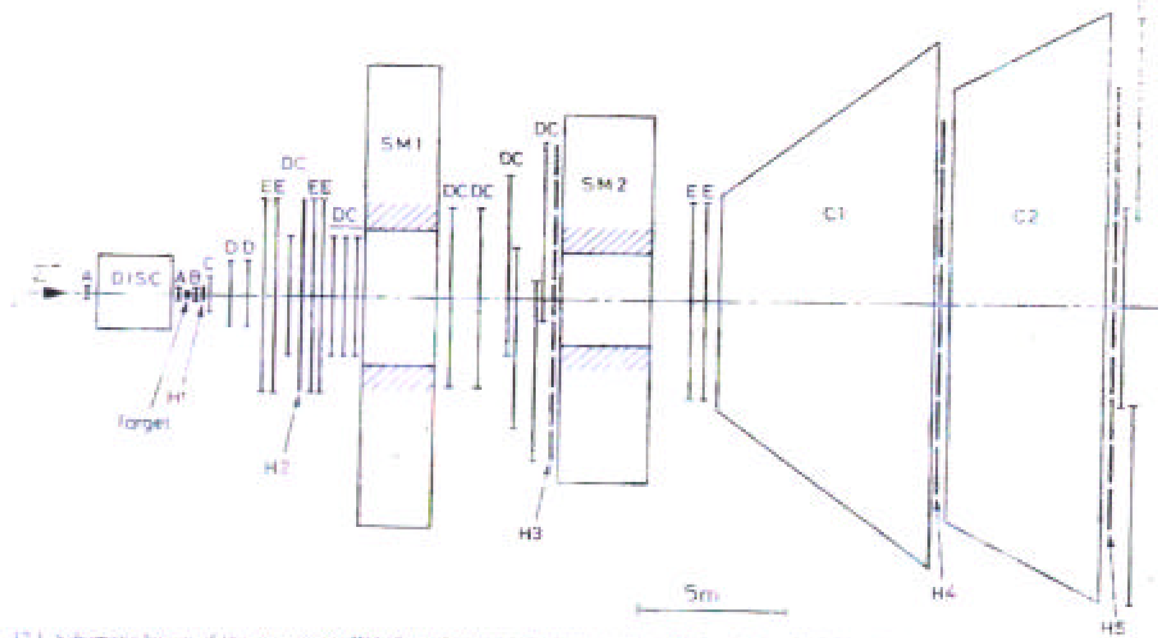

Fig. 12.1. Schematic layout of the experiment WA62 on charmed hyperons. A, B, C, D, E and F = MWPCs; DC = drift chambers; C1 and C2 = ... Čerenkov counters; H1–H5 = scintillator hodoscopes.

WA62: charm-strange baryons

Ξ_c^+: (82 ± 16) events (>6 sd)

for x>0.6, σ.B = (5.3 ± 2.0) μb/Be nucleus

lifetime = $(4.8^{+2.9}_{-1.8}) \times 10^{-13}$ s

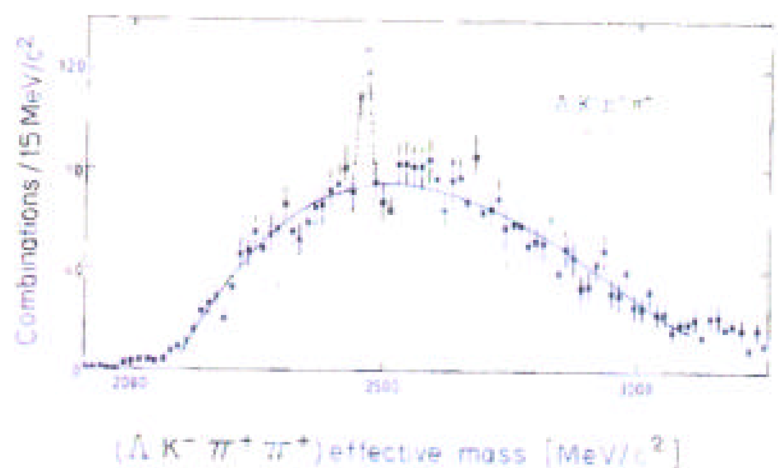

Fig. [illegible] The ($\Lambda K^- \pi^+ \pi^+$) effective mass distribution containing 4002 combinations made from 3352 events; points with error bars are data, lines are polynomial fits.

also Ω_c^0: 3 events in $\Xi^- K^- \pi^+ \pi^+$

WA62: U particles

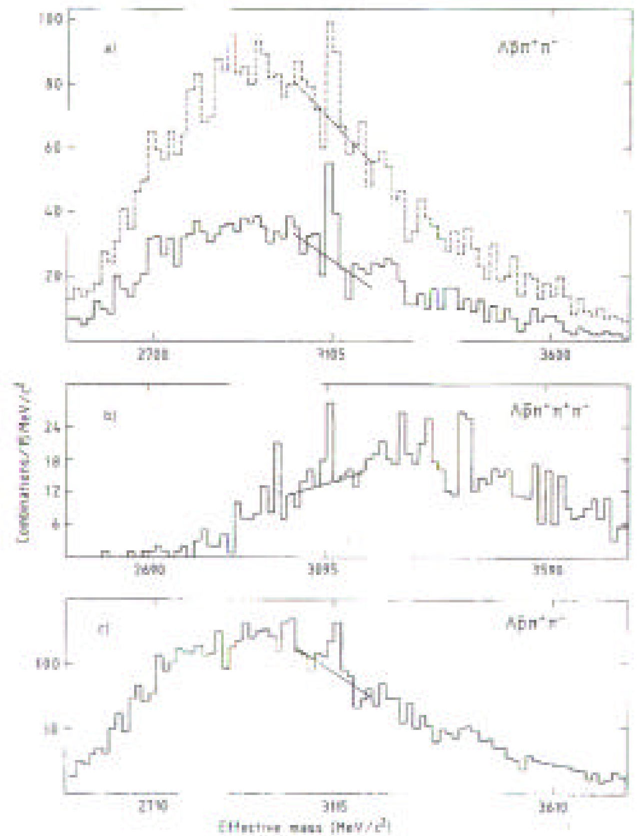

Fig. 2. Effective mass distributions. The dashed histogram in (a) shows the initial sample. The straight lines represent the background estimates given in the text. A vertical line on the figures corresponds to the same mass value in all three plots, however the bin limits do not coincide.

WA42/2

Improved DISC; improved acceptance for high-mass states; liquid argon and lead-glass detectors; gas Cerenkov for K/π separation.

Ξ^- / Σ^+ beam at 116 GeV/c

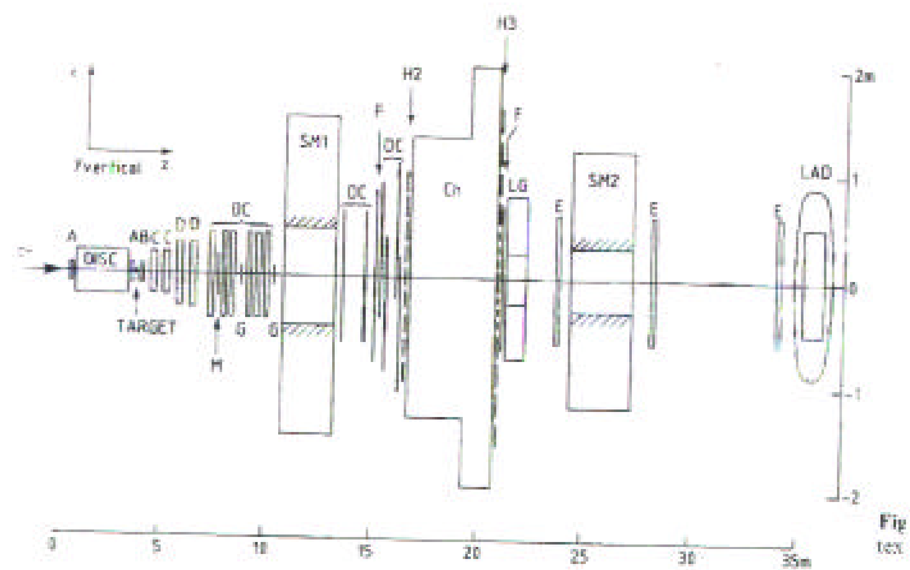

Fig

WA42/2: hyperon radiative decays

$\Sigma^+ \to p\gamma$ ~155 events $BR=(2.46^{+0.30}_{-0.35})\times10^{-3} / \Sigma^+ \to p\pi^0$

Z.Phys.C28,495 (1985)

$\Lambda \to n\gamma$ 23.7 events $BR=(1.02 \pm 0.33)\times10^{-3} / \Lambda \to \text{all}$

Z.Phys.C30,201 (1986)

$\Xi^- \to \Sigma^-\gamma$ 9.4 events $BR=(2.3 \pm 1.0)\times10^{-4} / \Xi^- \to \Lambda\pi^-$

Z.Phys.C35,143 (1987)

WA42/2: Ξ, Ω, Ξ^*, Ω^* production

$\Omega^*(2251)$ & $\Omega^*(2384)$ resonances.

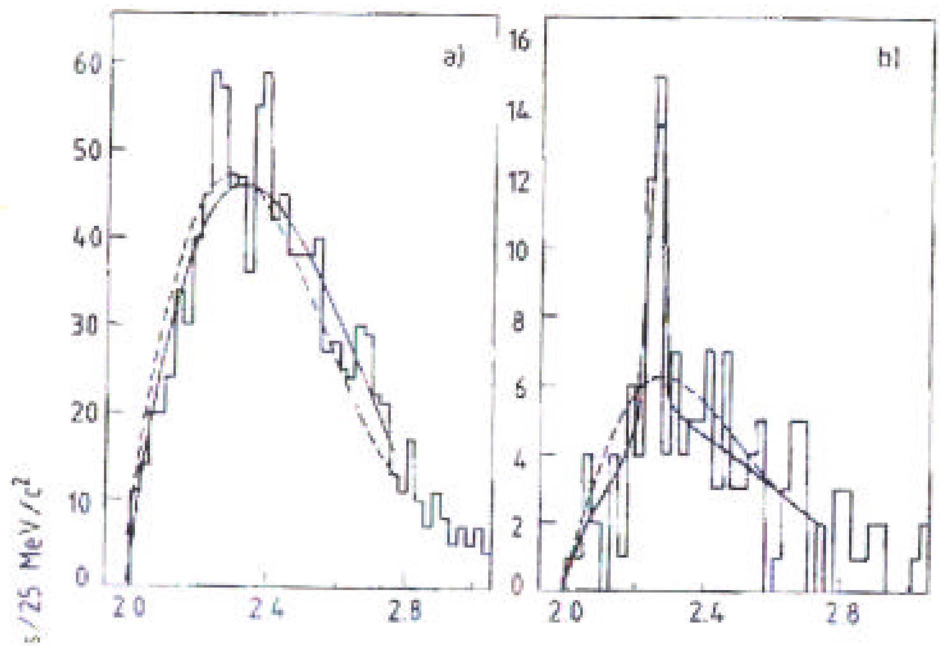

(b) with additional K^+/K^0

Fermilab Charged Hyperon Beam: E-715

Polarization of Σ^- ; asymmetries of: $\Sigma^- \rightarrow n e^- \bar{\nu}$

Magnetic moment of Σ^- using $n e^- \bar{\nu}$ and $n\pi^-$ decay modes.

Polarization of Ξ^- ; magnetic moment of Ξ^-

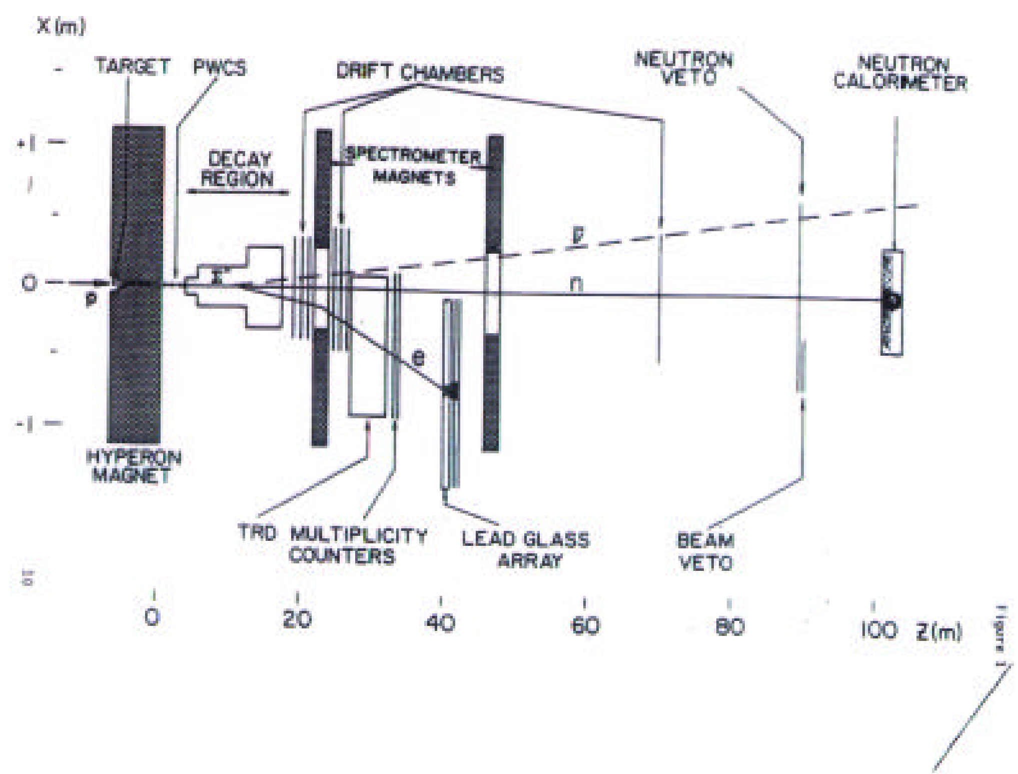

Fermilab Charged Hyperon Beam: E-761

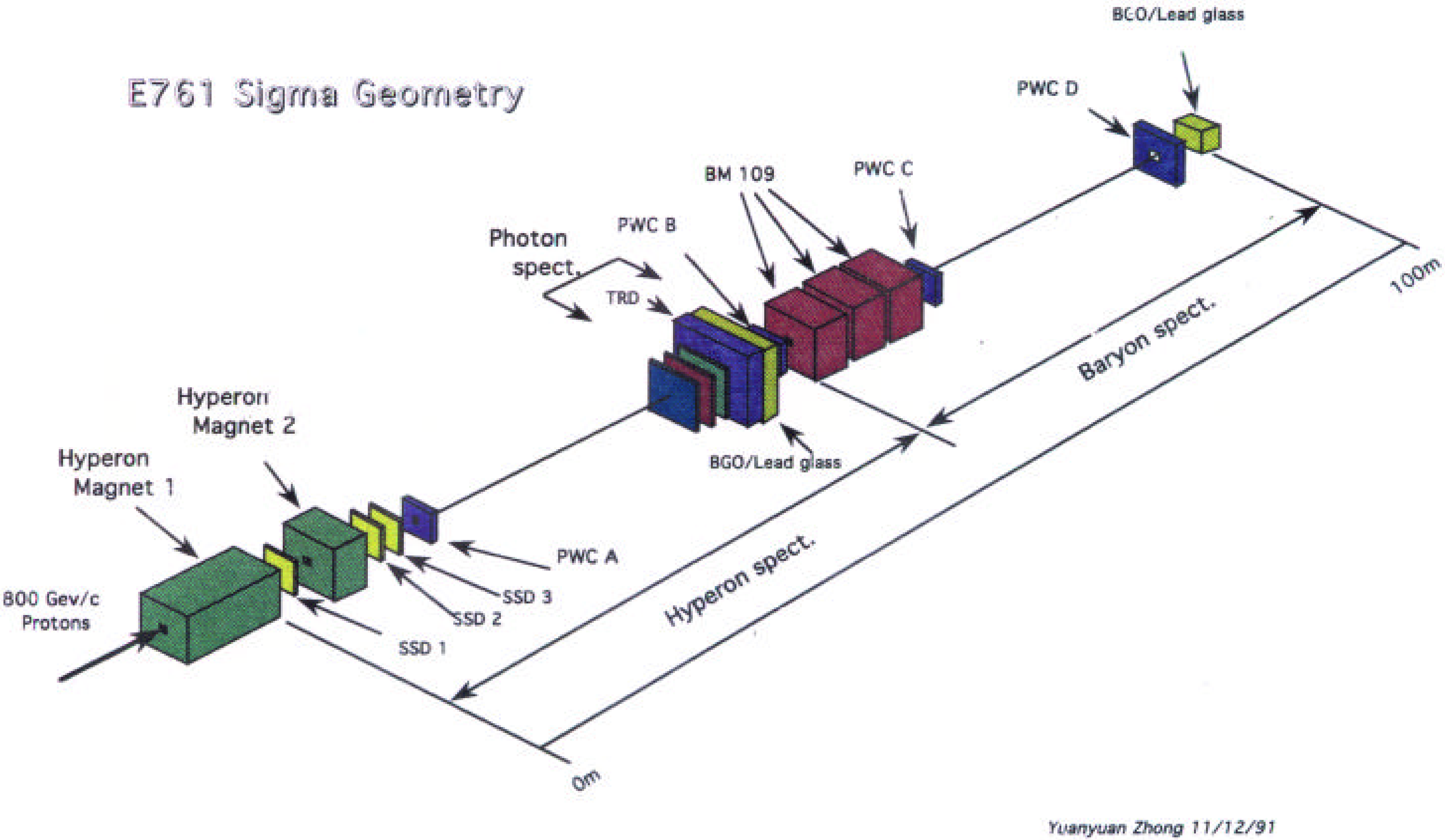

Fermilab Charged Hyperon Beam: E-761

Hyperon radiative decays:

α and BR: $\Sigma^+ \to p\gamma$; BR: $\Xi^- \to \Sigma^-\gamma$; upper limit: $\Omega^- \to \Xi^-\gamma$

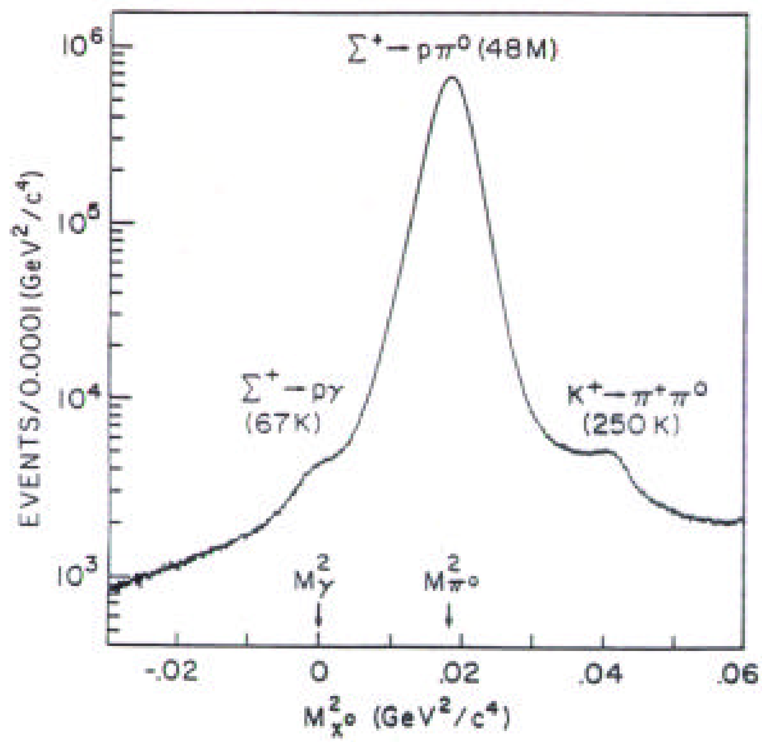

FIGURE 2. Event distribution of the mass squared of the missing neutral particle (X^+) for the hypothesis $\Sigma^+ \to pX^+$ for all candidates.

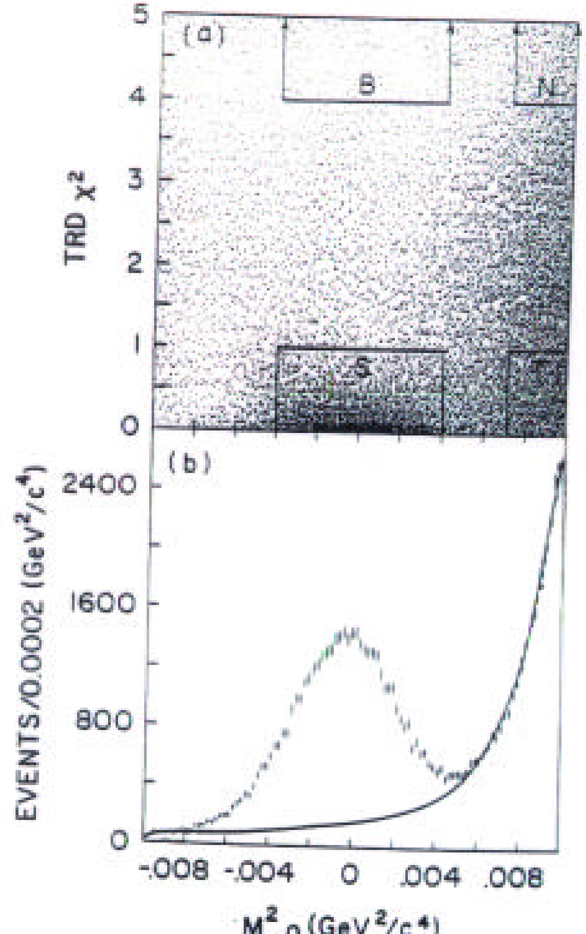

FIGURE 3. (a) Scatter plot of the TRD χ^2 described in the text vs the recoiling missing mass squared [$M^2_{X^+}$] for all events in the interval [$-0.01 < M^2_{X^+} < 0.01$ (GeV^2/c^4)] showing the four regions discussed in the text. (b) The missing mass squared distribution for all events with TRD

Fermilab Charged Hyperon Beam: E-761

Polarization and magnetic moments of Σ^+ and Σbar^-

Magnetic moment precession by channeling[111]

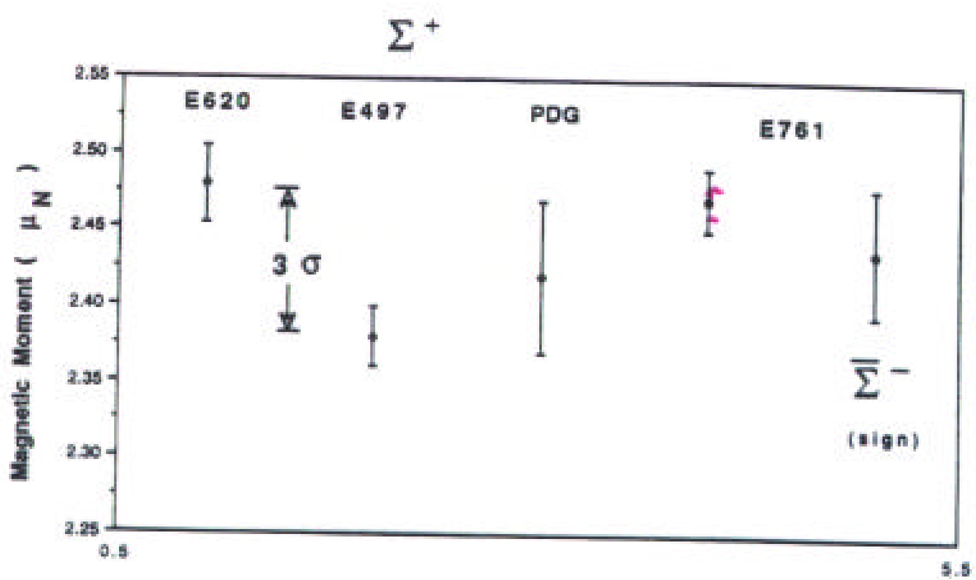

Figure 4.4: Σ^+ and $\bar{\Sigma}^-$ Magnetic Moment.